Giant spin splitting and its origin in methylhydrazinium lead halide perovskites

Nikhilesh Maity ⬤,[*] Ravi Kashikar, S. Lisenkov ⬤, and I. Ponomareva[†]
Department of Physics, University of South Florida, Tampa, Florida 33620, USA

Spin splitting, or removal of spin degeneracy in the electronic energy band/level, is often a measure of spin-orbit coupling strength and a way to manipulate spin degrees of freedom. We use first-principles simulations to predict giant spin splitting in methylhydrazinium lead halide (MHyPbX$_3$, MHy = CH$_3$NH$_2$NH$_2$, X = Br and Cl) hybrid organic-inorganic perovskites. The values can reach up to 408.0 meV at zero Kelvin and 281.6 meV at room temperature. The origin of the effect is traced to the large distortion of PbX$_3$ framework, driven primarily by Pb ions in the ferroelectric Γ^{3-} mode. The Pb displacements consist of a combination of polar and antipolar arrangements and result in up to 39.2 meV/atom enhancement of the spin-orbit coupling energy in the polar phase of the materials. The spin-orbit coupling gives origin to persistent spin textures in MHyPbX$_3$, which are desirable for applications in spintronics and quantum computing. Our findings reveal an additional functionality for hybrid organic-inorganic perovskite and open a way for the design of more materials with giant spin splitting.

Spin splitting is defined as the removal of spin degeneracy in the energy level of an isolated system or an energy band of a solid. It often originates from the relativistic effect of spin-orbit coupling (SOC) and was originally investigated by Dresselhaus [1] and Rashba *et al*. [2]. As a result, the effect carries their names. The SOC contributes a weak perturbation to the Hamiltonian of the system, which is proportional to $(\nabla V \times \mathbf{p}) \cdot \boldsymbol{\sigma}$, where V is the crystal potential, $\mathbf{p}$ is the momentum operator, and $\boldsymbol{\sigma}$ is the spin operator. Consequently, the effect originates from the presence of a (local) electric field, which could be due to the lack of inversion symmetry in bulk material [1], interfacial asymmetry in heterostructures [3], or even local asymmetry in centrosymmetric compounds [4]. The effect leads to spin-momentum locking and intriguing physical manifestations, which include intrinsic spin-Hall effect [5], gate-controlled spin precession [6], (inverse) spin galvanic effects, photogalvanic effects [7], and chiroptic effects [8]. These are believed to be promising for emerging spin-orbitronic devices that rely on manipulation of the spin degrees of freedom by electrical, optical, or magnetic means [5,9]. Spin splitting can also serve as a measure of SOC strength, which gives origin to many exotic phenomena, such as the switchable tunneling anomalous Hall effect (TAHE) [10,11] with ferroelectric polarization and tunneling anisotropic magnetoresistance (TAMR) [12,13] with magnetization.

Naturally, these intriguing effects and their emergent and potential applications rely on strong spin-momentum coupling and large spin splitting, which in turn originate from large SOC term [5,14,15]. For example, for room temperature applications it is desirable to have a material that exhibits spin splitting in excess of 30 meV. Unfortunately, being weak

relativistic effect SOC typically is not strong enough and so far only a handful of materials exhibited experimentally measurable or technologically significant values. One example is polar semiconductor BiTeI, which possesses spin splitting up to 100 meV [15]. The large value in BiTeI is attributed to the loss of inversion symmetry. Another example is cleaved topological insulator Bi$_2$Se$_3$, which exhibits Rashba spin splitting of up to 180 meV, which originates from band-bending induced potential gradient [16]. Rashba spin splitting is defined as the difference between the energy value at the momentum offset and time reversal invariant momentum point in materials whose free-electron bands are split by the Rashba Hamiltonian $H_R = \alpha_R \boldsymbol{\sigma} \cdot (\mathbf{k} \times \hat{\mathbf{n}})$, where k is the crystal momentum and $\hat{\mathbf{n}}$ is the unit vector along the symmetry axis, while α_R is the Rashba coefficient that quantifies the strength of SOC. In ferroelectric GeTe, Rashba spin splitting of 227 meV has been predicted computationally [17]. This huge spin splitting in GeTe is due to the unusual ordering of the bands near the Fermi surface that, combined with the small band gap, amplifies the effects of spin-orbit interaction [17]. Figure 1(a) compiles spin splitting values from the literature.

It should be mentioned that spin splitting can occur also in the absence of SOC in some antiferromagnetic materials. For example, in antiferromagnetic materials lacking θI symmetry (θ represents time reversal and I represents spatial inversion symmetry) and belonging to the magnetic space group of type III spin splitting can exist without SOC [18]. Likewise, altermagnets can exhibit spin splitted bands in absence of SOC owing to a special arrangement of spins and crystal symmetries [19].

Recently, the hybrid organic-inorganic perovskite with chemical formula ABX$_3$, having an organic molecule on the A site and, in some cases, organic ligands on the X site, are in the focus of scientific attention [20]. Along with their electronic and optoelectronic device applications [21–23], their low yield strain [24] offers an opportunity

---

*Contact author: nikhileshm@usf.edu
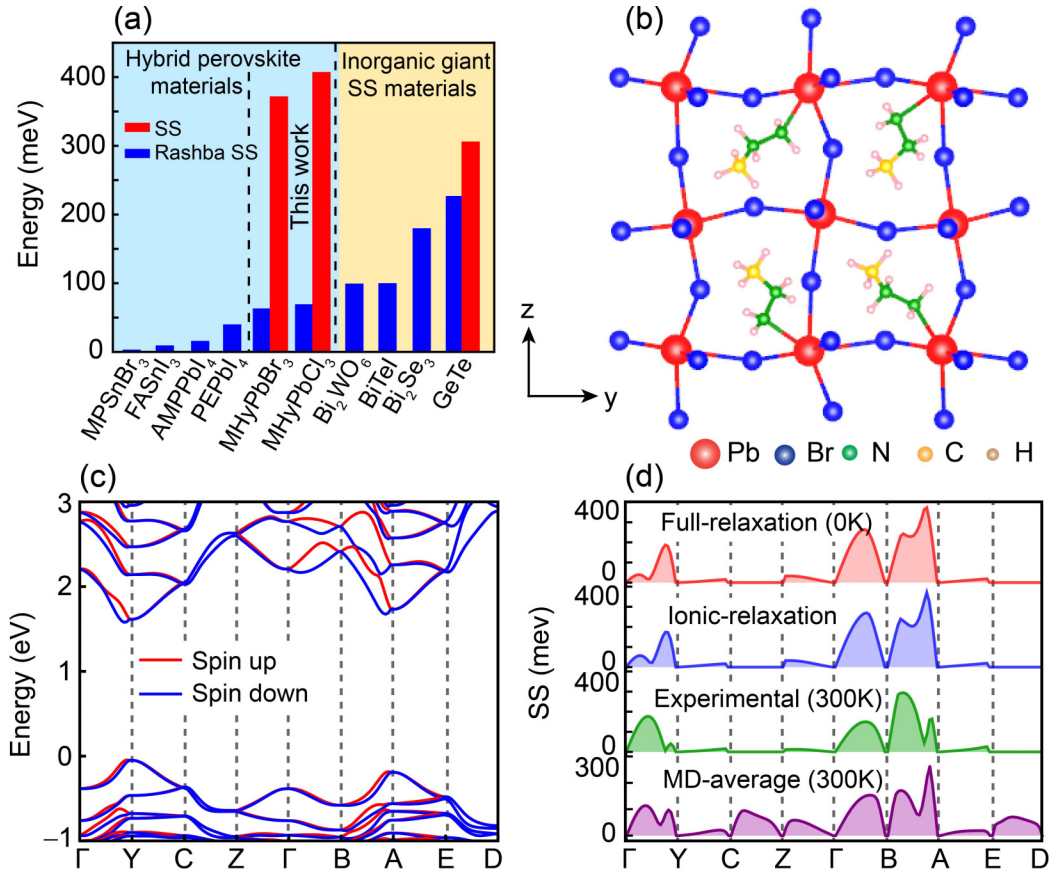†Contact author: iponomar@usf.edu

FIG. 1. (a) (Rashba) spin splitting for some representative materials from literature [15–17,23,28,42–44] and our spin splitting data in conduction band. (b) Crystal structure and (c) electronic band structure for $P2_1$ phase of MHyPbBr$_3$. (d) Spin splitting in conduction band along different directions in the momentum space for MHyPbBr$_3$ structures as obtained from different relaxation schemes of $P2_1$ phase.

to realize emerging devices, such as foldable, bendable, stretchable, and wearable devices [25]. For example, MAPbI$_3$ (where $MA = CH_3NH_3$) was realized as a flexible nonvolatile memory device [26] and flexible diffusive memristor for artificial nociceptors [27]. However, these materials typically exhibit rather mediocre spin splitting [see Fig. 1(a)]. Among the largest values reported so far is Rashba spin splitting of 40 meV, which was reported for two dimensional hybrid organic-inorganic perovskites, (PE)$_2$PbI$_4$ (where $PE = C_6H_5C_2H_4NH_3$) [28]. Recently, the new hybrid organic-inorganic perovskites MHyPbX$_3$, where MHy is methylhydrazinium molecule $CH_3NH_2NH_2$ and X is Br or Cl, have been experimentally synthesized [29,30]. The MHyPbBr$_3$ undergoes a phase transition from high temperature nonpolar Pm$\bar{3}$m phase to low temperature polar $P2_1$ phase at 418 K, while MHyPbCl$_3$ undergoes polar $Pb2_1$m to polar $P2_1$ phase transition at 342 K on cooling down. Both materials are known to exhibit strong octahedral distortions due to presence of large-sized MHy molecule (ionic radius 2.64 Å) in comparison with other hybrid perovskites [29,30]. Along with the large distortions, the presence of heavy element (Pb) on the B site suggests that this material could exhibit large or even giant spin splitting. Moreover, this material is also ferroelectric, which could offer the advantage of Rashba ferroelectricity cofunctionality [23]. Having the band gap in the visible region (for example 2.58 eV for MHyPbBr$_3$ [30]), these materials are also promising for optoelectronics applications. In this work,

we use first-principles DFT calculations with the aims (i) to predict giant spin splitting of MHyPbBr$_3$ and MHyPbCl$_3$; (ii) to reveal its fundamental origin; (iii) to report the unique spin textures in both MHyPbBr$_3$ and MHyPbCl$_3$, which are not present in inorganic materials with giant spin splitting.

We used first-principles density functional theory (DFT) based calculations as implemented in Vienna ab initio simulation package (VASP) [31,32]. The projector augmented wave (PAW) pseudopotential [33,34] and Perdew-Burke-Ernzerhof (PBE) [35] with D3 dispersion corrections as proposed by Grimme *et al.* [36] were used for the calculations. The energy cutoff of plane wave basis was set to 600 eV. For integration inside the Brillouin zone, we chose Γ-centered Monkhorst-Pack [37] k-point mesh of $8 \times 4 \times 4$ for both compounds. The structural relaxations were carried out using a conjugate gradient algorithm until the ionic forces were less, 5 meV Å^{-1}. All the electronic structure calculations were performed including SOC. For spin texture calculations, we used a 15×15 k-point mesh for a given plane in the reciprocal space. A dense k-point mesh of 21×21 has been used for the k$_x$-k$_z$ plane to clearly visualize the persistence spin texture. The polarization of the systems was calculated using modern theory of polarization as developed by King-Smith and Vanderbilt [38]. To avoid ambiguity due to polarization quantum in the calculation, we constructed a rotodistortion path as proposed in Ref. [39]. The ISOTROPY suite was used for the space group determination [40].

It has been established in the literature [41] that full structural relaxation using DFT does not always accurately predict structures which are not the ground state, which could lead to erroneous predictions for many properties, including spin splitting and related effects. It has previously been shown that for hybrid organic inorganic perovskites, *ab initio* molecular dynamics (AIMD) provides results which match experimental ones most closely [23]. We utilized such AIMD approach within the NVT ensemble, simulated using a Nose-Hoover thermostat. The run was initialized using the experimental structures with ionic positions fully relaxed. We simulated 12.5 ps using 1 fm time step. The last 10 ps of the run were used to compute the thermal average structure. For completeness, we also computed the structure by using full structural relaxation, ionic relaxation only (keeping lattice parameters equal to those in the experiment), and the experimentally obtained structure provided in Refs. [29,30].

We first use DFT calculations to predict the ground state structures of both $MHyPbBr_3$ and $MHyPbCl_3$. For that, the experimentally reported structures from Refs. [29,30] are subjected to full structural relaxation as outlined above. Both $MHyPbBr_3$ and $MHyPbCl_3$ retained their experimentally reported space groups of $P2_1$. A comparison between computational and experimental structural parameters is given in Table S1 of Supplemental Material [45]. The structural files are provided in Ref. [46]. The structural visualization of the $P2_1$ phase of $MHyPbBr_3$ and $MHyPbCl_3$ are given in Figs. 1(b) and S1(a), respectively. For $MHyPbCl_3$, we also investigate high-temperature polar phase $Pb2_1m$ (visualized in Fig. S1(b)). The spontaneous polarization of the $MHyPbBr_3$ ground state is $5.66 \mu C/cm^2$. For $MHyPbCl_3$ it is $6.44 \mu C/cm^2$ for $P2_1$ phase and $7.96 \mu C/cm^2$ for $Pb2_1m$ phase (see Fig. S2 of SM), which is in agreement with the recent computational results [47].

Next, we compute electronic structures of $MHyPbBr_3$ and $MHyPbCl_3$ taking into account SOC. Figure 1(c) gives the electronic structure of $P2_1$ phase of $MHyPbBr_3$, while data for other phases and materials are given in Fig. S3. The blue and red colours indicate bands with opposite spins. The band gaps for $MHyPbBr_3$ and $MHyPbCl_3$ in the monoclinic phases are 1.6 eV and 2.1 eV, respectively. In both materials, the valence band maximum (VBM) and conduction band minimum (CBM) occurs around Y(0.5, 0, 0). Furthermore, in $MHyPbBr_3$($MHyPbCl_3$), the eigenvalues of lowermost conduction band and uppermost valence band around A(0.5, 0, 0.5) are 95.2(90.0) meV greater and 138.4(151.7) meV lesser than that of Y, which allows for indirect transition between these two points. The partial density of states (Fig. S4) reveals that the valence bands near the Fermi level are dominated by X-p and Pb-s orbitals. The conduction bands near the Fermi level are formed primarily from Pb-p orbitals. The band structures reveal the presence of spin splitting in these materials. To quantify such spin splitting we computed the energy difference between the spin splitted bands along different directions in the Brillouin zone and report it in Fig. 1(d) for $MHyPbBr_3$ and in Fig. S5(a) for $MHyPbCl_3$. The data reveal giant spin splitting in conduction band, which can reach 372.6 and 408.0 meV for $MHyPbBr_3$ and $MHyPbCl_3$, respectively. These values of spin splitting are among the largest (likely the largest) reported in the literature so far to the best of our knowledge.

To eliminate the possibility that the giant spin splitting is an artifact of simulations, we computed spin splitting for the structures obtained from other relaxation techniques described in the method section, which, in addition, allows us to assess the temperature evolution of spin splitting. Figures 1(d) and S5(a) show a comparison of the spin splitting in conduction band between such simulations and reveal that all of them predict giant values for spin splitting. The AIMD data corresponds to 300 K and indicates that the maximum spin splitting in conduction band decreases only slightly (down to 281.6 meV) at finite temperatures, which is promising for potential applications.

To understand the origin of such giant spin splitting in $MHyPbX_3$, we take advantage of computations and decompose spin splitting into the contributions from MHy molecule and PbX_3 framework. For that, we first construct the centrosymmetric phase ($Pmma$) of the material using PSEUDO [48]. Next, we connect such centrosymmetric phase to the given noncentrosymmetric phase of the material ($P2_1$ phase, for example). A roto-distortion path is generated between the two, which consists of a rotation of the MHy molecule and distortion of PbX_3 framework. Such roto-distortion path is then "decomposed" into two. One of them contains only the rotation of the molecules and keeps the framework ions in their centrosymmetric positions. Another one includes only distortion of the framework and keeps the ions of the molecules in their centrosymmetric positions. These two paths quantify the contributions of the molecule and frameworks, respectively, to the structural distortions associated with the noncentrosymmetric phases [49,50]. For structures along each of the paths, we compute band structures and associated spin splitting. The same symmetry directions in the Brillouin zone as shown in Fig. 1(c) were considered in each case. Figure 2(a) reports the evolution of the spin splitting at A'(0.34, 0.0, 0.5) point in conduction band of the Brillouin zone along the distortion path for $MHyPbBr_3$. The evolution of spin splitting in conduction band for $MHyPbCl_3$ is given in Fig. S5(b). It reveals that the spin splitting in $MHyPbX_3$ is dominated by the framework.

Next, we aim to find out if there is a particular structural distortion of the framework that gives origin to the giant spin splitting. For that, the structural distortion associated with the framework is decomposed into individual modes using ISODISTORT [51,52]. The molecules are kept in their centrosymmetric positions. The framework distortion is made up of four Γ modes: Γ^{1-}, $\oplus\Gamma^{1+}$, $\oplus\Gamma^{3-}$, $\oplus\Gamma^{3+}$. The amplitude of these modes is given in Fig. 2(b) and reveals that Γ^{3-} mode has the largest amplitude. This is also the only ferroelectric mode in this material. To quantify the contributions of these different modes to spin splitting, we compute spin splitting associated with a condensation of each individual mode while keeping the molecules in their centrosymmetric positions. The data are given in Fig. 2(d) and reveal that it is the ferroelectric Γ^{3-} mode that is responsible for the giant spin splitting in this family of materials. Figure 2(c) visualizes ionic displacements associated with Γ^{3-} mode. The mode is dominated by Pb displacements, which are arranged in both polar and antipolar patterns. To elucidate the mechanism behind
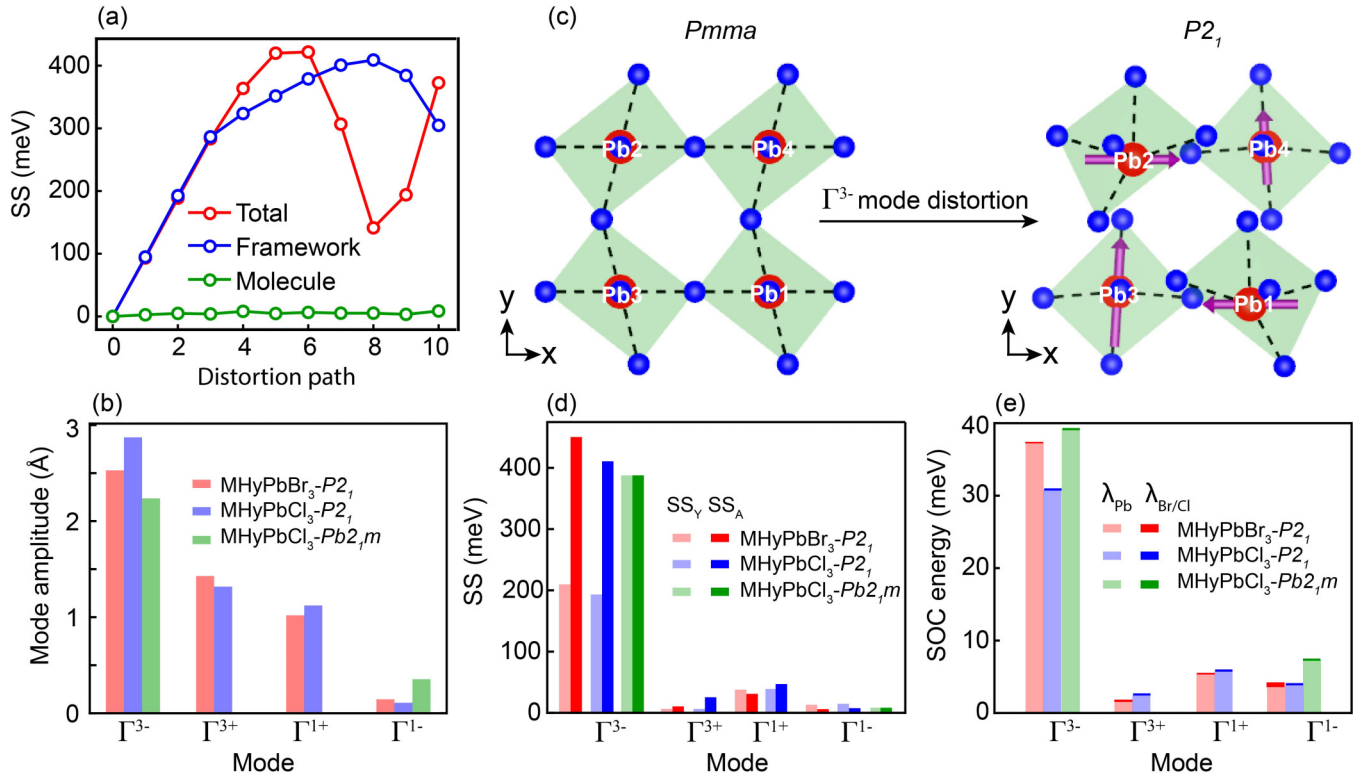
FIG. 2. (a) Decomposition of the spin splitting in conduction band at A′(0.34, 0.0, 0.5) point in Brillouin zone of MHyPbBr$_3$ into contributions from the molecule and framework. (b) Amplitude of structural distortions in different modes of $Pb2_1m$ and $P2_1$ phases of MHyPbBr$_3$ and MHyPbCl$_3$. (c) The atomic displacements in the Γ^{3-} mode in $P2_1$ phase of MHyPbBr$_3$. (d) The mode decomposition of spin splitting around Y and A high symmetry points (SS$_Y$ and SS$_A$) in conduction band. (e) The effective SOC energies for Pb, Br, and Cl atoms in different distortion modes.

ferroelectric mode-driven giant spin splitting, we compute effective SOC energies, E_{SOC}, inside the augmentation spheres centered around a given ion as outlined in Refs. [53,54]. The difference in these energies between the given phase and the centrosymmetric phases, $\lambda(i) = E_{SOC}(i) - E_{SOC}^{cs}(i)$, for different types of ions are reported in Fig. 2(e). There exists a drastic enhancement of E_{SOC} for the Pb ions in Γ^{3-} mode, which explains why this polar mode is responsible for the giant spin

splitting. Thus, our calculations reveal that highly distorted PbX$_3$ framework results in large polar displacement of Pb, which causes strong enhancement of spin-orbit interactions, resulting in giant spin splitting. Since the large framework distortion is believed to be caused by the large size of MHy molecule, we believe that our insight will lead to the design of more hybrid organic-inorganic perovskites with giant spin splitting.
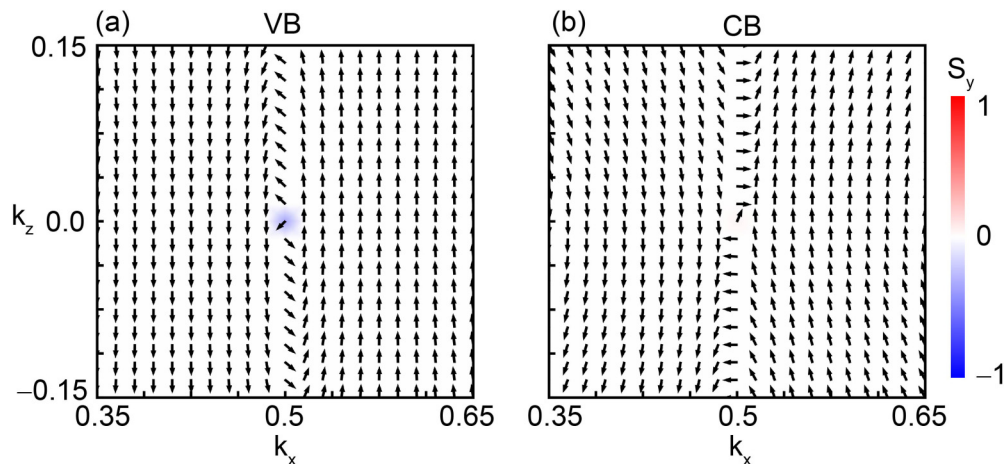

FIG. 3. The spin texture of (a) valence band (VB) and (b) conduction band (CB) of MHyPbBr$_3$ around Y high symmetry point in the k_x-k_z plane, obtained from DFT.

TABLE I. Effective masses (m_x, m_y, and m_z) and spin-splitting strengths (α_x, α_z, β, γ_x, and γ_z) in unit of free electron mass and eVÅ, respectively, for valence band (VB) and conduction band (CB).

Compound		m_x	m_y	m_z	α_x	α_z	β	γ_x	γ_z
MHyPbBr$_3$	CB	0.27	0.28	0.91	0.1	1.4	0.02	0.01	0.38
	VB	0.37	0.32	0.71		0.05	0.45	0.04	0.04	−0.01
MHyPbCl$_3$	CB	0.36	0.36	1.15	0.1	1.34	0.02	0.06	0.28
	VB	0.44	0.39	0.72	−0.01	0.22	0.03	−0.04	−0.04

Spin splitting is known to give origin to spin textures, which are vectorial representations of expectation values of the spin components in momentum space. In ferroelectrics, they can be controlled by the application of an electric field, thanks to the coupling between spin textures and electric polarization [55]. Figure 3 shows the spin textures in k_x-k_z plane for valence band and conduction band around Y high symmetry point of MHyPbBr$_3$, which are persistent in the vicinity of CBM and VBM. The persistent spin textures provide a long spin lifetime of carriers, which is highly desirable for spin–orbitronics [5]. For other plane, the spin textures of MHyPbBr$_3$ and MHyPbCl$_3$ are given in Figs. S8, S9, and S10. To elucidate the origin of the persistent nature of spin textures in MHyPbBr$_3$ and MHyPbCl$_3$ we develop effective Hamiltonian using the method of invariants [56]. The point group corresponding to $P2_1$ space group is C_2. The wave vector point group for both Y and A points is also C_2. The transformation rules for wave vector $\boldsymbol{k}$ and spin $\boldsymbol{\sigma}$ in C_2 point group are given in Table S2. From the common invariant terms, the effective Hamiltonian is

$$H = \frac{(\hbar k_x)^2}{2m_x} + \frac{(\hbar k_y)^2}{2m_y} + \frac{(\hbar k_z)^2}{2m_z} + \alpha_x k_x \sigma_x + \alpha_z k_x \sigma_z$$
$$+ \beta k_y \sigma_y + \gamma_x k_z \sigma_x + \gamma_z k_z \sigma_z, \qquad (1)$$

where k_i are components of wave vector, m_i are effective masses, and σ_i are the Pauli spin matrices. α_x, α_z, β, γ_x, and γ_z are spin-momentum coupling parameters that can be obtained by fitting the eigenvalues of the Hamiltonian of Eq. (1) to the values computed from DFT. The fitting details are provided [45]. The parameters obtained for the vicinity of the Y point are listed in Table I. An analysis of the parameters' strengths indicate that the effective masses are $\boldsymbol{k}$-dependent and have larger values along the k_z direction. In case of the MHyPbX$_3$, we find that among the parameters that control spin splitting, the largest values are for α_z followed by γ_z, and the other two terms are significantly smaller. For the valence band, α_z is nearly order of magnitude larger than other

parameters. In this case the Hamiltonian can be approximated as $\frac{(\hbar k_x)^2}{2m_x} + \frac{(\hbar k_y)^2}{2m_y} + \frac{(\hbar k_z)^2}{2m_z} + \alpha_z k_x \sigma_z$ with the eigenvalues of $E_\pm = \frac{(\hbar k_x)^2}{2m_x} + \frac{(\hbar k_y)^2}{2m_y} + \frac{(\hbar k_z)^2}{2m_z} \pm \alpha_z k_x$ and the associated expectation value for the spin $\langle \sigma_\pm \rangle = (0, 0, \pm 1)$. The independence of the expectation value of the $\boldsymbol{k}$-vector (except for the sign flip due to the change of the outer branch from E_+ to E_- as the direction of k_x flips) explains the persistent nature of the spin textures. The finite values of other parameters alter the spin texture near the CBM and VBM slightly toward a quasi-persistent one. In summary, we used DFT calculations to predict giant spin splitting in MHyPbX$_3$ hybrid organic-inorganic perovskites. The values up to 408.0 meV were obtained for spin splitting at zero Kelvin and up to 281.6 meV in MHyPbCl$_3$ at room temperature. The origin of such a large value was traced to the Pb displacements in the ferroelectric Γ^{3-} mode triggered by large framework distortion required to accommodate large MHy molecule. The displacement can reach 0.92 Å, which combined with the large Z of Pb leads to the strong enhancement of spin-orbit interaction energy, up to 39.2 meV/atom. Moreover, the SOC leads to the development of persistent spin textures in the momentum space, which are known to significantly enhance spin relaxation time, and, therefore, are very valuable for applications in spintronics and quantum computing. Thus, our study reveals that MHyPbX$_3$ is a ferroelectric semiconductor with giant spin splitting and persistent spin textures in momentum space. All of these are the key properties for emerging applications such as in efficient spin field effect transistors, valley spin valve, and barrier of ferroelectric tunnel junctions. In addition, being hybrid organic-inorganic perovskites these materials are relatively soft and flexible, which could bring the realization of flexible, foldable, and even wearable spintronics. The knowledge on the fundamental origin of the giant spin splitting in MHyPbX$_3$ is likely to promote design of other hybrid materials with giant spin splitting and could open up a new direction in hybrid perovskites research. In particular, identifying molecule-framework combinations which promote large polar distortions of heavy elements could be one potential design avenue.

[1] G. Dresselhaus, Spin-orbit coupling effects in zinc blende structures, Phys. Rev. **100**, 580 (1955).

[2] E. I. Rashba and V. I. Sheka, Digital access to Scholarship at Harvard, *Symmetry of Energy Bands in Crystals of Wurtzite Type II. Symmetry of Bands with Spin-Orbit Interaction Included* (Harvard Library, 1959).

[3] Y. A. Bychkov and É. I. Rashba, Properties of a 2D electron gas with lifted spectral degeneracy, JETP Lett. **39**, 78 (1984).

[4] X. Zhang, Q. Liu, J.-W. Luo, A. J. Freeman, and A. Zunger, Hidden spin polarization in inversion-symmetric bulk crystals, Nat. Phys. **10**, 387 (2014).

[5] A. Manchon, H. C. Koo, J. Nitta, S. M. Frolov, and R. A. Duine, New perspectives for Rashba spin–orbit coupling, Nat. Mater. **14**, 871 (2015).

[6] S. Datta and B. Das, Electronic analog of the electro-optic modulator, Appl. Phys. Lett. **56**, 665 (1990).

[7] J. Wang, H. Lu, X. Pan, J. Xu, H. Liu, X. Liu, D. R. Khanal, M. F. Toney, M. C. Beard, and Z. V. Vardeny, Spin-dependent photovoltaic and photogalvanic responses of optoelectronic devices based on chiral two-dimensional hybrid organic–inorganic perovskites, ACS Nano **15**, 588 (2021).

[8] P. C. Sercel, Z. V. Vardeny, and A. L. Efros, Circular dichroism in non-chiral metal halide perovskites, Nanoscale **12**, 18067 (2020).

[9] M. Kepenekian, R. Robles, C. Katan, D. Sapori, L. Pedesseau, and J. Even, Rashba and Dresselhaus effects in hybrid organic–inorganic perovskites: From basics to devices, ACS Nano **9**, 11557 (2015).

[10] N. Nagaosa, J. Sinova, S. Onoda, A. H. MacDonald, and N. P. Ong, Anomalous Hall effect, Rev. Mod. Phys. **82**, 1539 (2010).

[11] A. V. Vedyayev, M. S. Titova, N. V. Ryzhanova, M. Y. Zhuravlev, and E. Y. Tsymbal, Anomalous and spin Hall effects in a magnetic tunnel junction with Rashba spin-orbit coupling, Appl. Phys. Lett. **103**, 032406 (2013).

[12] A. N. Chantis, K. D. Belashchenko, E. Y. Tsymbal, and M. van Schilfgaarde, Tunneling anisotropic magnetoresistance driven by resonant surface states: First-principles calculations on an Fe(001) surface, Phys. Rev. Lett. **98**, 046601 (2007).

[13] J. Moser, A. Matos-Abiague, D. Schuh, W. Wegscheider, J. Fabian, and D. Weiss, Tunneling anisotropic magnetoresistance and spin-orbit coupling in Fe/GaAs/Au tunnel junctions, Phys. Rev. Lett. **99**, 056601 (2007).

[14] E. Lesne, Y. Fu, S. Oyarzun, J. C. Rojas-Sánchez, D. C. Vaz, H. Naganuma, G. Sicoli, J.-P. Attané, M. Jamet, E. Jacquet, J.-M. George, A. Barthélémy, H. Jaffrès, A. Fert, M. Bibes, and L. Vila, Highly efficient and tunable spin-to-charge conversion through Rashba coupling at oxide interfaces, Nat. Mater. **15**, 1261 (2016).

[15] K. Ishizaka, M. S. Bahramy, H. Murakawa, M. Sakano, T. Shimojima, T. Sonobe, K. Koizumi, S. Shin, H. Miyahara, A. Kimura, K. Miyamoto, T. Okuda, H. Namatame, M. Taniguchi, R. Arita, N. Nagaosa, K. Kobayashi, Y. Murakami, R. Kumai, Y. Kaneko, Y. Onose, and Y. Tokura, Giant Rashba-type spin splitting in bulk BiTeI, Nat. Mater. **10**, 521 (2011).

[16] P. D. C. King, R. C. Hatch, M. Bianchi, R. Ovsyannikov, C. Lupulescu, G. Landolt, B. Slomski, J. H. Dil, D. Guan, J. L. Mi, E. D. L. Rienks, J. Fink, A. Lindblad, S. Svensson, S. Bao, G. Balakrishnan, B. B. Iversen, J. Osterwalder, W. Eberhardt, F. Baumberger, and P. Hofmann, Large tunable Rashba spin splitting of a two-dimensional electron gas in Bi_2Se_3, Phys. Rev. Lett. **107**, 096802 (2011).

[17] D. Di Sante, P. Barone, R. Bertacco, and S. Picozzi, Electric control of the giant Rashba effect in bulk GeTe, Adv. Mater. **25**, 509 (2013).

[18] L.-D. Yuan, Z. Wang, J.-W. Luo, E. I. Rashba, and A. Zunger, Giant momentum-dependent spin splitting in centrosymmetric low-z antiferromagnets, Phys. Rev. B **102**, 014422 (2020).

[19] L. Šmejkal, A. B. Hellenes, R. González-Hernández, J. Sinova, and T. Jungwirth, Giant and tunneling magnetoresistance in unconventional collinear antiferromagnets with nonrelativistic spin-momentum coupling, Phys. Rev. X **12**, 011028 (2022).

[20] L. Wei, A. Stroppa, Z.-m. Wang, and S. Gao, *Hybrid Organic-Inorganic Perovskites* (John Wiley & Sons, 2020).

[21] S. D. Stranks and H. J. Snaith, Metal-halide perovskites for photovoltaic and light-emitting devices, Nat. Nanotechnol. **10**, 391 (2015).

[22] N.-G. Park, M. Grätzel, T. Miyasaka, K. Zhu, and K. Emery, Towards stable and commercially available perovskite solar cells, Nat. Energy **1**, 16152 (2016).

[23] R. Kashikar, P. S. Ghosh, S. Lisenkov, A. Stroppa, and I. Ponomareva, Rashba effects in lead-free ferroelectric semiconductor $[CH_3PH_3]SnBr_3$, Phys. Rev. Mater. **6**, 104603 (2022).

[24] Q. Tu, D. Kim, M. Shyikh, and M. G. Kanatzidis, Mechanics-coupled stability of metal-halide perovskites, Matter **4**, 2765 (2021).

[25] S.-J. Kim and J.-S. Lee, Flexible organic transistor memory devices, Nano Lett. **10**, 2884 (2010).

[26] C. Gu and J.-S. Lee, Flexible hybrid organic–inorganic perovskite memory, ACS Nano **10**, 5413 (2016).

[27] H. Patil, H. Kim, K. D. Kadam, S. Rehman, S. A. Patil, J. Aziz, T. D. Dongale, Z. A. Sheikh, M. K. Rahmani, M. F. Khan, and D.-k. Kim, Flexible organic–inorganic halide perovskite-based diffusive memristor for artificial nociceptors, ACS Appl. Mater. Interfaces **15**, 13238 (2023).

[28] Y. Zhai, S. Baniya, C. Zhang, J. Li, P. Haney, C.-X. Sheng, E. Ehrenfreund, and Z. V. Vardeny, Giant Rashba splitting in 2D organic-inorganic halide perovskites measured by transient spectroscopies, Sci. Adv. **3**, e1700704 (2017).

[29] M. Mączka, A. Gagor, J. K. Zareba, D. Stefanska, M. Drozd, S. Balciunas, M. Šimėnas, J. Banys, and A. Sieradzki, Three-dimensional perovskite methylhydrazinium lead chloride with two polar phases and unusual second-harmonic generation bistability above room temperature, Chem. Mater. **32**, 4072 (2020).

[30] M. Mączka, M. Ptak, A. Gagor, D. Stefanska, J. K. Zareba, and A. Sieradzki, Methylhydrazinium lead bromide: Noncentrosymmetric three-dimensional perovskite with exceptionally large framework distortion and Green photoluminescence, Chem. Mater. **32**, 1667 (2020).

[31] G. Kresse and J. Furthmüller, Efficient iterative schemes for *ab initio* total-energy calculations using a plane-wave basis set, Phys. Rev. B **54**, 11169 (1996).

[32] G. Kresse and J. Furthmüller, Efficiency of *ab-initio* total energy calculations for metals and semiconductors using a plane-wave basis set, Comput. Mater. Sci. **6**, 15 (1996).

[33] P. E. Blöchl, Projector augmented-wave method, Phys. Rev. B **50**, 17953 (1994).

[34] G. Kresse and D. Joubert, From ultrasoft pseudopotentials to the projector augmented-wave method, Phys. Rev. B **59**, 1758 (1999).

[35] J. P. Perdew, K. Burke, and M. Ernzerhof, Generalized gradient approximation made simple, Phys. Rev. Lett. **77**, 3865 (1996).

[36] S. Grimme, Semiempirical GGA-type density functional constructed with a long-range dispersion correction, J. Comput. Chem. **27**, 1787 (2006).

[37] H. J. Monkhorst and J. D. Pack, Special points for Brillouin-zone integrations, Phys. Rev. B **13**, 5188 (1976).

[38] R. D. King-Smith and D. Vanderbilt, Theory of polarization of crystalline solids, Phys. Rev. B **47**, 1651 (1993).

[39] M. Kingsland, P. S. Ghosh, S. Lisenkov, and I. Ponomareva, Structural, electrical, and electromechanical properties of inverse hybrid perovskites from first-principles: The case of $(CH_3NH_3)_3OI$, J. Phys. Chem. C **125**, 8794 (2021).

[40] H. T. Stokes and D. M. Hatch, *FINDSYM*: program for identifying the space-group symmetry of a crystal, J. Appl. Crystallogr. **38**, 237 (2005).

[41] K. Frohna, T. Deshpande, J. Harter, W. Peng, B. A. Barker, J. B. Neaton, S. G. Louie, O. M. Bakr, D. Hsieh, and M. Bernardi, Inversion symmetry and bulk Rashba effect in methylammonium lead iodide perovskite single crystals, Nat. Commun. **9**, 1829 (2018).

[42] A. Stroppa, D. Di Sante, P. Barone, M. Bokdam, G. Kresse, C. Franchini, M.-H. Whangbo, and S. Picozzi, Tunable ferroelectric polarization and its interplay with spin–orbit coupling in tin iodide perovskites, Nat. Commun. **5**, 5900 (2014).

[43] F. Wang, H. Gao, C. de Graaf, J. M. Poblet, B. J. Campbell, and A. Stroppa, Switchable Rashba anisotropy in layered hybrid organic–inorganic perovskite by hybrid improper ferroelectricity, npj Comput. Mater. **6**, 183 (2020).

[44] H. Djani, A. C. Garcia-Castro, W.-Y. Tong, P. Barone, E. Bousquet, S. Picozzi, and P. Ghosez, Rationalizing and engineering Rashba spin-splitting in ferroelectric oxides, npj Quantum Mater. **4**, 51 (2019).

[45] See Supplemental Material at http://link.aps.org/supplemental/10.1103/PhysRevMaterials.8.L091402 for details of crystal structures and polarizations for all phases; comparison of structural parameters; electronic band structures and spin splitting along the symmetry direction for conduction band and valence band for all phases; density of states; comparison of spin splitting for $MHyPbCl_3$ structure from different relaxation scheme; decomposition of spin splitting for $MHyPbCl_3$; energy and temperature profile for AIMD simulations; electronic band structure for total distortion, framework distortion and molecule rotation; spin textures for different planes in the momentum space; comparison the eigenvalues from effective Hamiltonian and DFT.

[46] S. Lisenkov, USFmatscilab/MHyPbX3, https://github.com/USFmatscilab/MHyPbX3.

[47] P. Srivastava, S. Maity, and V. Srinivasan, Guest-induced phase transition leads to polarization enhancement in $MHyPbCl_3$, arXiv:2309.10386.

[48] C. Capillas, E. S. Tasci, G. de la Flor, D. Orobengoa, J. M. Perez-Mato, and M. I. Aroyo, A new computer tool at the Bilbao crystallographic server to detect and characterize pseudosymmetry, Z. Kristallogr. **226**, 186 (2011).

[49] D. Di Sante, A. Stroppa, P. Jain, and S. Picozzi, Tuning the ferroelectric polarization in a multiferroic metal–organic framework, J. Am. Chem. Soc. **135**, 18126 (2013).

[50] A. Stroppa, P. Jain, P. Barone, M. Marsman, J. M. Perez-Mato, A. K. Cheetham, H. W. Kroto, and S. Picozzi, Electric control of magnetization and interplay between orbital ordering and ferroelectricity in a multiferroic metal–organic framework, Angew. Chem., Int. Ed. **50**, 5847 (2011).

[51] H. T. Stokes, S. van Orden, and B. J. Campbell, *ISOSUBGROUP*: An internet tool for generating isotropy subgroups of crystallographic space groups, J. Appl. Crystallogr. **49**, 1849 (2016).

[52] B. J. Campbell, H. T. Stokes, D. E. Tanner, and D. M. Hatch, *ISODISPLACE*: A web-based tool for exploring structural distortions, J. Appl. Crystallogr. **39**, 607 (2006).

[53] S. Steiner, S. Khmelevskyi, M. Marsmann, and G. Kresse, Calculation of the magnetic anisotropy with projected-augmented-wave methodology and the case study of disordered $Fe_{1-x}Co_x$ alloys, Phys. Rev. B **93**, 224425 (2016).

[54] E. v. Lenthe, E. J. Baerends, and J. G. Snijders, Relativistic regular two-component Hamiltonians, J. Chem. Phys. **99**, 4597 (1993).

[55] C. M. Acosta, A. Fazzio, G. M. Dalpian, and A. Zunger, Inverse design of compounds that have simultaneously ferroelectric and Rashba cofunctionality, Phys. Rev. B **102**, 144106 (2020).

[56] L. L. Tao and E. Y. Tsymbal, Perspectives of spin-textured ferroelectrics, J. Phys. D: Appl. Phys. **54**, 113001 (2021).